RSC Advances

PAPER

View Article Online
View Journal | View Issue

Cite this: *RSC Adv.*, 2026, **16**, 14183

Strategic integration of carbon nanotubes over the redox-active surfaces of $FeCo_2S_4$ as an electrode material for developing high-efficiency supercapacitor devices

Muhammad Yahya Haroon, [a] Ali Raza Tahir,[a] Muhammad Usman,[a] Abdul Shakoor, [a] Muhammad Luqman, [a] Shahid M. Ramay,[b] Muhammad Farooq Saleem[cd] and Shahid Atiq *[a]

Accelerating both electrical and ionic conductivity of spinel sulfides (AB_2S_4) presents a challenge that demands an urgent solution to improve their electrochemical properties for effective energy storage strategies. The need to develop electrode materials has been a significant step forward for the scientific community in enhancing electrochemical performance for supercapacitor applications. Therefore, incorporating carbon nanotubes (CNTs) into spinel sulfides could be an excellent option, serving as a model for new electrodes. To investigate this, $FeCo_2S_4$ spinel sulfide was combined with CNTs *via* hydrothermal and solvothermal synthesis. A series of $FeCo_2S_4$/CNTs composites with 0, 3, 6, and 9 wt% CNTs were successfully prepared and confirmed *via* X-ray diffraction (XRD) technique. Meanwhile, Field Emission Scanning Electron Microscopy (FESEM) revealed topographical features, including web-like structures of the highest CNTs treated sample, with significantly improved interconnectivity that enhances ion and electron transport. The $FeCo_2S_4$/9% CNTs electrode delivered an efficient electrochemical response, with a specific capacity of 1059.62 C g^{-1} at 10 A g^{-1}, an energy density of 66.22 Wh kg^{-1}, and a power density of 2250 W kg^{-1}, while also retaining 98.8% of its initial capacity after 10k cycles. Electrochemical analyses further confirmed a hybrid charge-storage process, with low charge transfer resistance (5.15 Ω), stable conductivity (0.13 S cm^{-1}), and a short relaxation time (0.010 s), yielding a maximum cation mobility of 3.81 × 10^{-10} m^2 V^{-1} s^{-1} and a rate constant of 6.03 × 10^{-8} cm s^{-1} at 5.82 mA g^{-1}. The fabricated asymmetric pseudocapacitive device facilitated the maximum energy and power density values of around 63.15 Wh kg^{-1} and 10 800 W kg^{-1}, respectively, in 1 M KOH electrolyte. These findings suggest that CNT-assisted $FeCo_2S_4$ nanocomposites exhibit remarkable redox activity and transport properties, making them promising electrodes for high-performance supercapacitors.

Received 20th December 2025
Accepted 29th January 2026

DOI: 10.1039/d5ra09850e

rsc.li/rsc-advances

1. Introduction

In support of global sustainable development, research organizations are bridging the gap between energy production and consumption, thereby developing efficient and affordable energy conversion and storage solutions.[1–6] In this pursuit, supercapacitors (SC) have gained widespread attention as alternatives to batteries, thanks to their exceptional features such as high intrinsic power density (PD), excellent retention capacity even at high current densities (I_m), fast rechargeability, notable specific capacitance (C_{sp}), and wide operating voltage.[7–9] Despite their rapid growth, SCs still face challenges in achieving high energy density (ED), which requires significant advancements.[7,8] In principle, the electrochemical performance of SC is primarily determined by its charge-storage mechanism. In this context, the electrochemical double-layer capacitance is commonly observed in high-specific-surface-area (SSA) carbon-based electrode materials, which involves rapid electrostatic adsorption at the electrode–electrolyte interface.[9–12] In contrast, transition metal-based compounds such as oxides (TMOs) and sulfides (TMS) typically exhibit pseudocapacitive (PC) behavior due to faradaic redox activities.[13–15] The presence or absence of functional groups and oxygen/sulfur vacancies are the major differences between these two categories of charge storage, determining whether an electrode material is redox-active or chemically inert.

[a]*Centre of Excellence in Solid State Physics, University of the Punjab, Lahore-54590, Pakistan. E-mail: satiq.cssp@pu.edu.pk*

[b]*Physics and Astronomy Department, College of Science, King Saud University, P. O. Box 2455, Riyadh 11451, Saudi Arabia*

[c]*SPIN-Lab Centre for Microscopic Research on Matter, University of Silesia in Katowice, 75 Pulku Piechoty 1A, 41-500, Chorzow, Poland*

[d]*Institute of Chemistry, University of Silesia in Katowic, 9 Szkolna Str., 40-007, Katowice, Poland*

Therefore, to bridge the gap with batteries with an aim to elevate the ED and PD together, recent research has focused on hybrid electrode materials, leading to the development of hybrid capacitors (HCs).[14,16] These HCs combine high ED and ultrafast charge delivery, dominating the respective electrode components.[16,17] For this purpose, a spinel-structured (AB_2X_4) ternary TMS, $FeCo_2S_4$, has gained significant attention due to its favorable redox chemistry (Fe^{2+}/Fe^{3+}, Co^{2+}/Co^{3+}) and adaptable electronic properties.[18,19] Unlike similar oxides (*e.g.*, $FeCo_2O_4$), sulfur-rich $FeCo_2S_4$ provides better electrical conductivity, because of its low electron negativity compared to oxygen.[19–21] Additionally, compared to other ternary TMS such as $CuCo_2S_4$, $NiCo_2S_4$, and $ZnCo_2S_4$, the multiple valence states and abundance of naturally occurring Fe allow for a robust PC phenomenon.[22,23] Despite these outstanding features, however, $FeCo_2S_4$-based electrode materials have received limited electrochemical investigation.[24–29]

In this pursuit, Narwal *et al.* prepared $FeCo_2S_4$/MWCNTs nanocomposite *via* hydrothermal methods, reaching a C_{sp} around 432 F g^{-1} at about 0.5 A g^{-1} compared to pristine $FeCo_2S_4$. The fabricated asymmetric SC exhibited an ED of 49.40 Wh kg^{-1} and a maximum PD of 20 kW kg^{-1}, with 93.94% retention over 5000 cycles. However, in his work, the influence of CNT integration was not investigated systematically along with lack in quantitative storage mechanisms such as capacitive and diffusive contributions and ion transport properties as well.[26] Another $FeCo_2S_4$@MXene nanocomposite was prepared *via in situ* growth and hydrothermal methods, exhibiting an excellent C_{sp} of approximately 2415.3 F g^{-1} and a notable cyclic stability of 90.50%. An assembled $FeCo_2S_4$@MXene//AC device in this study delivered the maximum ED of about 68 Wh kg^{-1} with a PD of 800 W kg^{-1}.[19] For clarity, a comparative study of a few more reported works on $FeCo_2S_4$-based materials is graphically displayed in Fig. 1(a), promoting their potential for HCs technology.[19,26,27,32,33] The above-mentioned reports displayed high C_{sp} but at the cost of complex synthesis and reliance on multiple substrates.[27–29] Collectively, these reports lack a comprehensive assessment of the ion-transport properties underlying improvements in energy storage capabilities, including ionic conductivity, transference number, cation mobility, and rate constants.[19,26–33]

Considering these research gaps, this study addresses them by incorporating CNTs into $FeCo_2S_4$ at different concentrations, offering an effective solution, as CNTs are known for their remarkable electrical conductivity ($\sim 10^4$ S cm^{-1}). The synergistic effect of the conductive CNT network modulates the redox-active sites of $FeCo_2S_4$, further preventing sulfur loss and phase changes.[26] In this context, a cost-effective solvothermal technique is used to successfully incorporate CNTs at varying loadings into pristine $FeCo_2S_4$ (PFCS), labeled FCS-I (3% CNTs), FCS-II (6% CNTs), and FCS-III (9% CNTs). In a nutshell, to our knowledge, this is the first FCS-based material-type study that provides a survey of ion transport properties underlying the systematic improvement in the charge storage capabilities of as-fabricated electrode series. Furthermore, the projected estimates of ionic properties, including sample-to-sample variation in ionic conduction, are coupled with assessments of the transference number, cation mobility, and the variation of exchange current density and rate constant. To further enhance the overall impact of this study from a practical life application perspective, an asymmetric device configuration was also established, yielding the maximum ED of 63.15 Wh kg^{-1} and a PD around 10 800 W kg^{-1}. To compare the achievements reported in the literature, Fig. 1(b) and the web plot depicted in Fig. 1(c) are shown to graphically distinguish them, highlighting the ion transport features as a unique aspect of this work.[19,26,27,32,33] In addition to this study, the success in developing sulfide-based monolayers and sheets, as well as the pillaring of MWCNTs, can be a beneficial approach for the development of high-efficiency energy storage devices.

2. Experimental portion

2.1. Materials and chemicals

The raw materials used to develop pristine iron cobalt sulfide and its composite samples with multiple CNTs loadings were purchased from different sources and were not further purified.

For example, the precursors are $Fe(NO_3)_3 \cdot 9H_2O$, $Co(NO_3)_3 \cdot 6H_2O$, and thiourea ($SC(NH_2)_2$), each with a purity of about 99.98%, were used in the development of the parent material and were purchased from Sigma Aldrich catalog #659258. In addition to this, the solvent (ethanol) used here and

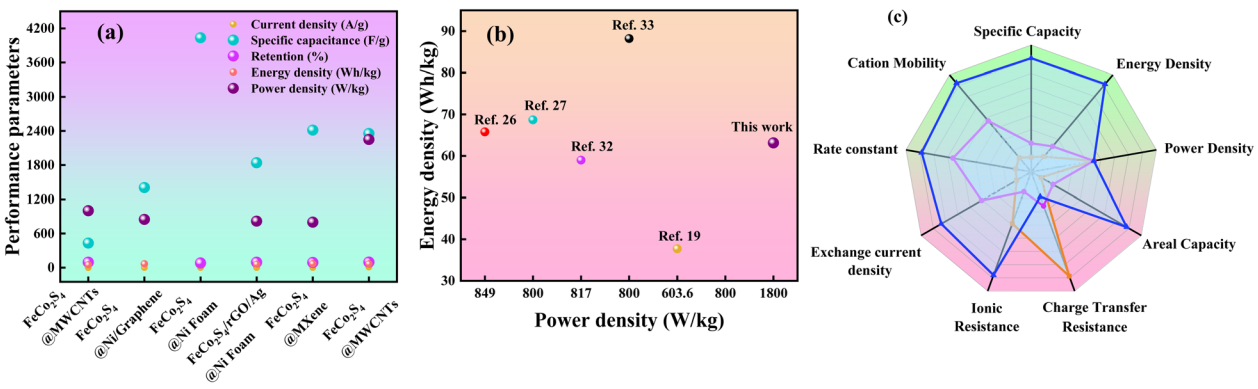

Fig. 1 (a) Graphical comparison of the difference performance parameters of various materials with our achievements, (b) Ragone plot of different materials, and (c) web plot representing the core focus of this study.

ammonium fluoride (NH_4F), with a purity of 99.99%, and the functionalized CNTs with a diameter of 10–20 nm and 10–30 μm length were purchased from Macklin Chemical Supplier.

2.2. Preparation of $FeCo_2S_4$ (PFCS)

A simple hydrothermal method was used to prepare the pure $FeCo_2S_4$ (FCS) with molar ratios of F : Co : S = 1 : 2 : 4. The nitrate precursors, $SC(NH_2)_2$ and NH_4F, with a purity of 99.99%, were used directly from the bottle without purification. Each chemical reagent, namely $Fe(NO_3)_3 \cdot 9H_2O$ and $Co(NO_3)_3 \cdot 6H_2O$, was weighed at 0.582 g (2.0 mmol) and 0.404 g (1 mmol), respectively, and dissolved in separate beakers containing 25 mL and 20 mL of DI water. $SC(NH_2)_2$ (0.304 g, 4.0 mmol) and NH_4F (0.148 g, 4.0 mmol) were added gradually with magnetic stirring at 250 rpm to the combined solution. This uniform solution was transferred into a thermally stable autoclave and heat-treated at 180 °C for 16 hours. After cooling, a suspension was formed, which was purified of impurities by centrifugation using DIW and ethanol several times. Thus, a precipitate was obtained that was dried at 70 °C for several hours in the Meilleur vacuum oven.

2.3. Preparation of $FeCo_2S_4$/CNTs

The solvothermal method was used to synthesize FCS@CNT composites at concentrations of 0% (100 mg), 3% (97 mg, 3 mg), 6% (94 mg, 6 mg), and 9% (91 mg, 9 mg). In parentheses, the values represent the weights of FCS and CNTs. The stoichiometrically weighed amounts were specified to sum to 100 mg of PFCS and CNTs. Specifically, the four samples created were labeled as PFCS (0% CNT), FCS-I (3% CNT), FCS-II (6% CNT), and FCS-III (9% CNT). This solvothermal process is more user-friendly and cost-effective for producing particles in the nanometer range, along with improved morphology and porosity. In this process, measured amounts of CNTs (0, 3, 6, and 9 mg) were mixed into FCS (100, 97, 94, and 91 mg) in 40 mL of ethanol and subjected to vigorous ultrasonic treatment combined with stirring at 250 rpm for 1 hour to ensure homogeneous dispersion. After forming the carbonaceous mixture, it was carefully poured into a thermally stable autoclave (Fig. 2) and heated at 95 °C in a muffle furnace for 1 h. Then, the obtained precipitate was collected after the autoclave cooled, washed several times with ethanol and DIW during centrifugation, and carefully dried.

2.4. Preparation of the electrode

The electrode fabrication involves several primary steps. It begins with carefully cutting the nickel foam (NF) substrate into 1 × 1.25 cm pieces. The reason for choosing NF over carbon cloth (CC) or metal foils is its low cost, notable conductivity, and electrochemical stability, which promote efficient conduction for the electrode material and electrolyte. To prepare the NF, pieces were immersed in an acidic solution comprising 13 mL of HCl in 37 mL of DIW. This solution helps remove contaminants and etch away the oxygen layer from the NF, thereby increasing surface roughness. Next, 85% active material, 10% binder (PVDF + DMF), and 5% activated carbon were mixed to prepare the slurry, which was then stirred vigorously for 8 hours. Herein, 10% binder was carefully added as per our lab optimizations and precautions to prepare the slurry. The binder (PVDF + DMF) facilitates excellent chemical adhesion of the

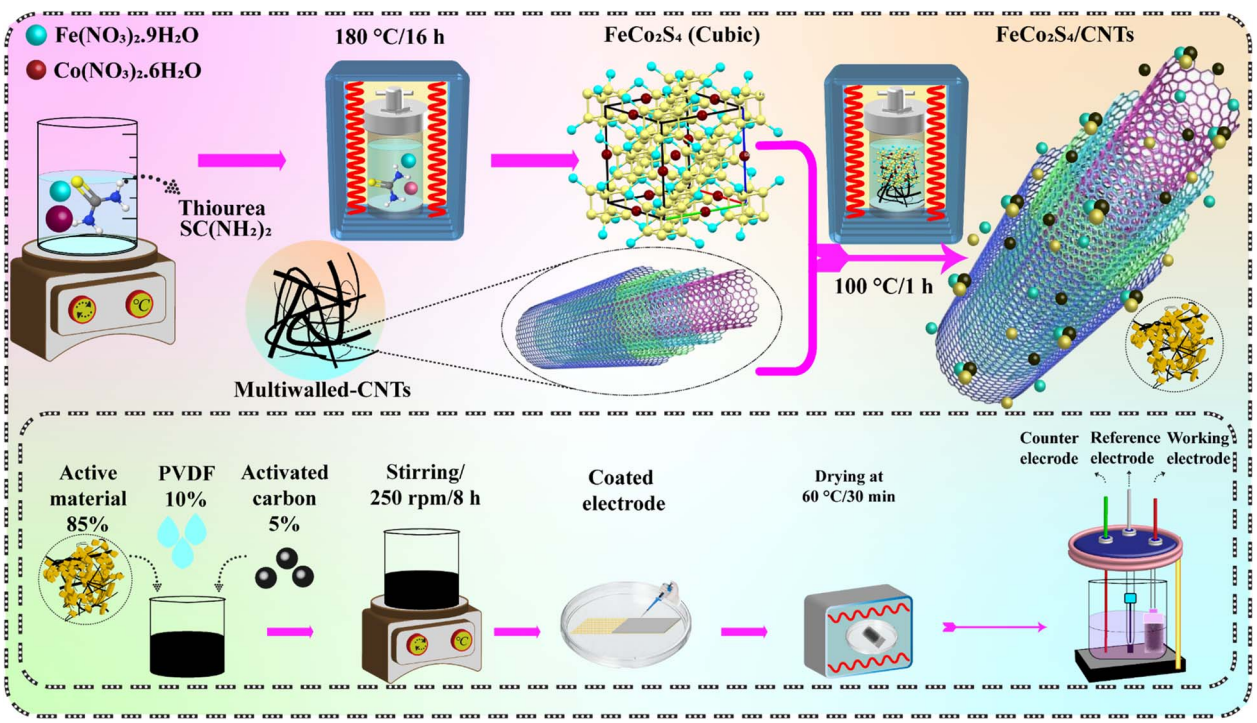

Fig. 2 Schematic profile of the sample's synthesis and electrode fabrication.

active material with NF and provides a wide electrochemical potential range. Furthermore, its addition ensures the mechanical stability of the fabricated material over repeated cycling, and the 10% binder solution is our optimized range, which ensures the stability of ion transport and limits internal resistance-related factors. Afterward, a Dragon pipette was carefully used to deposit the slurry onto the etched NF pieces. These coated NF dried at 60 °C for a few minutes before being used as an electrode for electrochemical testing, as shown in Fig. 2.

3. Results and discussion

3.1. Structural analysis

A structural analysis of PFCS and its composites with 0, 3, 6, and 9% CNT contents was conducted to identify the crystalline phase within the 2θ range of 15° to 70°, as illustrated in the XRD patterns in Fig. 3(a). The methodology proposed by B. D. Cullity was used to identify and index these patterns. The major peaks were observed at $2\theta = 21.10°$, 31.20°, 37.95°, 50.18°, and 55.10°, corresponding to the respective values of *hkl* of (220), (311), (400), (511), and (440), which showed a good match with the JCPDS reference code 47-1738 confirming the cubic spinel structure of PFCS with no standard diffraction card and good match with a binary phase Co_3S_4. In the meantime, the remaining peaks at 44.62°, 51.98°, and 76.45° were associated with diffraction probabilities for Ni with Miller indices (111), (200), and (220), respectively, originating from the nickel foam used as a substrate. It was also observed that the inclusion of CNTs did not affect the diffraction probabilities of associated planes in all samples. Matching these peaks with the exact crystal structure remains unresolved based on the literature survey of B. D. Cullity. Moreover, the crystal structure of PFCS was animated using VESTA software, with identical atomic positions in the unit cell, as displayed in Fig. 3(b). Additionally, the crystallite sizes of PFCS and FCS-III were estimated using Scherrer's equation, yielding values of 31 and 28.90 nm. The decrease in crystallite size is attributed to lattice contraction and a reduced nucleation rate of PFCS in the composite sample, owing to strong van der Waals interactions. In principle, the high surface energy and abundant nucleation sites of CNTs promote heterogeneous nucleation, leading to a greater number of nuclei with restricted growth dimensions. The presence of CNT functional groups further suppresses crystallite growth kinetics by anchoring the growing domains.[30,31] From this perspective, the electrochemical properties of FCS-III are expected to outperform those of PFCS.

3.2. Morphological and compositional analyses

The FESEM images were used at 25 000× magnification to examine the morphology, shape, and arrangement of microparticles in PFCS, FCS-I, FCS-II, and FCS-III electrode materials, as demonstrated in Fig. 4(a–d). The FESEM image in Fig. 4(a) revealed sharp morphological features of PFCS, with flake-like nanosheets combined with irregular nanoparticles. These flake-like nanosheets provide a high SSA, indicating potential for increased storage capacity due to greater interaction opportunities between electrolyte ions and the material. The image also reveals a significant porous structure in PFCS, evidenced by visible voids within the nanosheets and nanoparticles. This porosity can facilitate electrolyte ions in effectively engaging with exposed active sites, thereby maximizing electrochemical response. Additionally, the dense, agglomerated pattern of nanosheets and the clustering of nanoparticles may hinder efficient redox reactions and ion diffusion by restricting ion pathways. Nevertheless, the prominent features of this morphology are promising for future electrochemical applications.

Within this framework, the FESEM images of FCS-I, FCS-II, and FCS-III composites shown in Fig. 4(b–d) demonstrate key insights into CNTs integration with the PFCS matrix. The image of FCS-I clearly shows the growth of an interconnected fibrous network with significant nanoparticle agglomeration, as

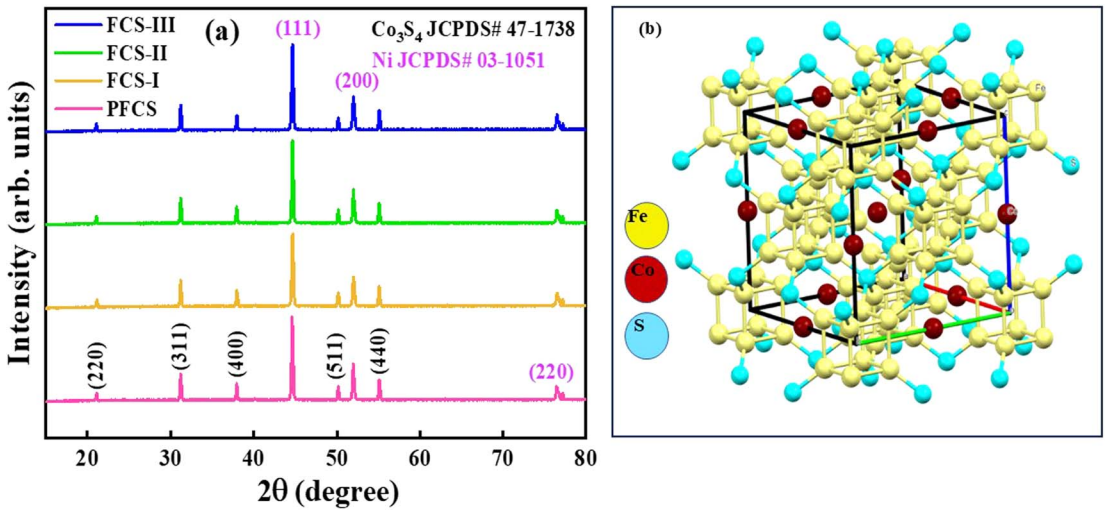

Fig. 3 (a) XRD patterns of PFCS, FCS-I, FCS-II, and FCS-III, and (b) crystal structure of PFCS.

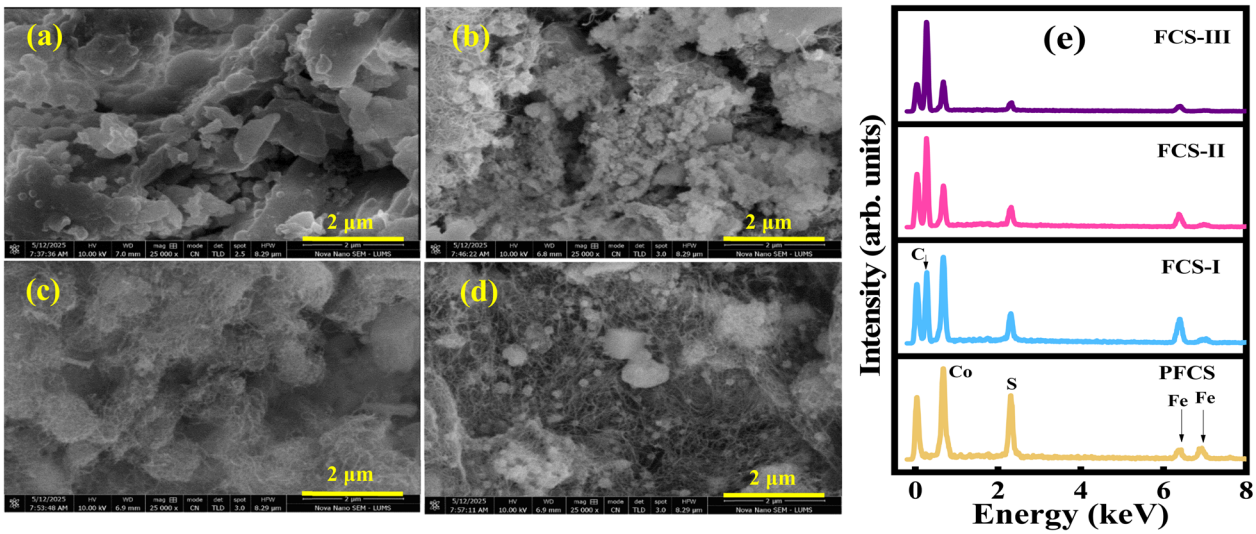

Fig. 4 (a–d) FESEM images of PFCS, FCS-I, FCS-II, and FCS-III, and (e) EDX spectra of as-synthesized materials.

illustrated in Fig. 4(b). This indicates CNTs incorporation into the parent material (PFCS). The cause of this agglomeration is a less-developed CNT network within the material due to a relatively low CNT concentration, which further limits electrochemical activities. Additionally, even with low CNT content, there is an improvement in conductivity, enhancing electron and ion transport, which is essential for electrochemical performance. In contrast, the FCS-II sample exhibits a dense, uniform CNT network anchored over the pure PFCS matrix, as seen in Fig. 4(c). The interconnected dense morphology and retained porosity of micro-particles can facilitate efficient electron transfer, leading to improved electrical conductivity and mechanical strength. However, the dense CNT coverage over the PFCS matrix reduces the number of active sites available for ion interaction and intercalation.

On the other hand, the FCS-III composite displays the most favorable morphological features among all samples, as portrayed in Fig. 4(d). The FESEM image unveiled a homogeneous, well-dispersed, web-like CNT network embedded within the PFCS micro-particles. This also confirms very little agglomeration along with an increased porosity level in the micro-particles, compared to all other samples. Additionally, the porous web-like structure is well-defined, indicating an electrochemically advantageous morphology that promotes rapid ion exchange, lower R_{ct} values, and efficient diffusion dynamics. All these outstanding morphological features suggest that FCS-III is the most enhanced electrode material for electrochemical applications and energy storage devices.

Elemental analysis was performed using EDX to verify the presence of constituent elements at the microscopic level and their weight percentages in the as-prepared PFCS and FCS/CNTs composites. The EDX spectra for all samples are shown in Fig. 4(e), with yellow, blue, pink, and magenta colors for PFCS, FCS-1, FCS-II, and FCS-III, respectively. Distinct peaks corresponding to Fe, Co, and S, along with carbon (C), were clearly observed, with no impurity peaks detected, confirming the exact composition of FCS. When CNTs were added, a prominent peak appeared in the EDX spectra of the PFCS/CNTs composites, and the C peak intensity increased with higher CNT content. Notably, the Fe, Co, and S peaks remained consistent across all samples, indicating successful synthesis of the PFCS and PFCS/CNTs composites. In this context, Table 1 presents the precise composition of all the prepared samples.

To quantify the porosity features estimated in PFCS and FCS-III using the Brunauer–Emmett–Teller (BET) technique by allowing the adsorption/desorption of nitrogen gas at 77 K. This experiment of PFCS and FCS-III resulted in two pairs of nitrogen adsorption and desorption isotherms, as depicted in Fig. 5, reflecting the type-IV isotherm, signifying the presence of meso and micro pores in these two materials.[34] The behaviour showed an increase when 9% CNTs were included, indicating the presence of additional diffusion channels. For instance, a pristine sample exhibited a maximum pore volume of 0.97 $cm^3\ g^{-1}$ and a BJH surface area of 29.27 $m^2\ g^{-1}$, while FCS-III provided the highest SSA of 68.62 $m^2\ g^{-1}$. In this way, the FCS-III appeared to be the best among all other electrode materials as an efficient electrode material to be used for high charge storage devices.

3.3. Electrochemical analysis

The CV provides crucial electrochemical investigations that help to elucidate how a fabricated electrode behaves when the system is subjected to a constant potential window. It provides

Table 1 Elemental composition of PFCS, FCS-I, FCS-II, and FCS-III

Sample	wt (%) Fe	wt (%) Co	wt (%) S	wt (%) C
PFCS	18.50	39.0	42.50	0
FCS-I	17.95	37.83	41.33	2.90
FCS-II	17.39	36.66	40.95	4.90
FCS-III	16.94	35.69	38.68	8.54

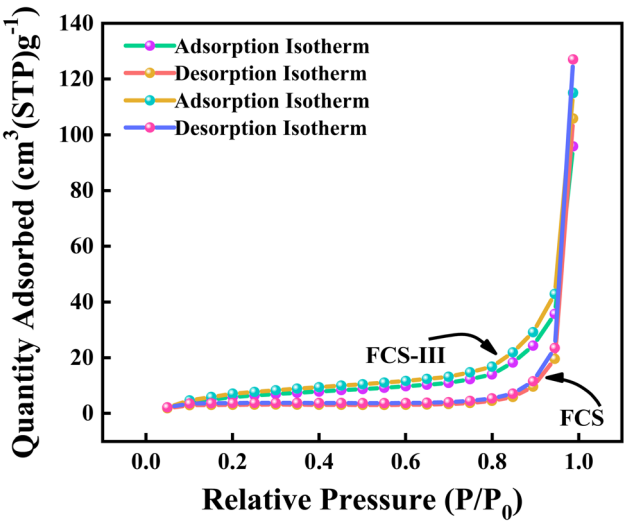

Fig. 5 Nitrogen adsorption/desorption isotherms of PFCS and FCS-III.

a detailed study of redox mechanisms, rate capability, and capacitive properties, all performed in potentiostat mode.[31–38] Consequently, Fig. 6(a–d) displays cyclic voltammograms (CVs) of PFCS, FCS-I, FCS-II, and FCS-III, conducted within an optimized range of 0 V to 0.43 V constant potential at scan rates (SRs) of 5, 7.5, 10, and 15 mV s^{-1}. In Fig. 6(a–d), the minimum activation potentials to initiate the redox reactions for PFCS, FCS-I, FCS-II, and FCS-III are observed at (0–28) V, (0–27) V, (0–25) V, and (0–24) V, respectively. Additionally, the obtained CVs, which maintain consistent shapes across all samples in Fig. 6(a–d) redox peaks without significant distortion of the electrode materials. Notably, the stable CVs and narrow peak potential separation (ΔE_p) even at high scan rates, suggest high reversibility, durability, and a long cycle life for the synthesized samples. The main reason for these results appears to be smooth contact at the electrode–electrolyte interface, indicating efficient ion migration into the porous channels of the electrode. Furthermore, in Fig. 6(a–d), the CVs exhibit faradaic processes, confirming the Co^{2+} to Co^{3+} conversions, as shown in chemical reactions eqn (1) and (2).

$$FeCo_2S_4 + OH^- \leftrightarrow FeCo_2S_4OH + e^- \quad (1)$$

$$FeCo_2S_4OH + e^- \leftrightarrow FeCo_2S_4 + OH^- \quad (2)$$

However, a minor shift in oxidation peaks (0.37–0.43 V) and reduction peaks (0.17–0.21 V) across SR (5–15 mV s^{-1}) was observed for all samples. This peak shift toward higher and lower potentials with increasing SR suggests highly reversible kinetics of PFCS-based electrode materials. It can also be explained that rapid charge transport occurs at higher scanning speeds compared to lower speeds. Additionally, the gradual incorporation of CNTs into PFCS increased the current, as shown on the *y*-axis of Fig. 6(a–d). These efficient electrochemical results are attributed to the synergistic effect of the strong interaction between CNTs and the PFCS active material.

Besides that, Fig. 6(e) shows a composite graph at the SR of 5 mV s^{-1}, providing a qualitative interpretation and comprehensive analysis of the electrochemical response for PFCS-based electrode materials. In Fig. 6(e), the obtained CVs at this SR display a duck-like profile along with a capacitive region (0–0.28 V) and non-capacitive features (oxidation peaks after 0.28 V and reduction peaks before 0.28 V), confirming battery-type behaviour. Additionally, Fig. 6(e) demonstrates that FCS-II and FCS-III exhibit more prominent electrochemical responses compared to PFCS and FCS-I, due to the higher concentration of CNTs. It is worth noting that the CNTs' 3D scaffold significantly facilitates charge transportation by providing large exposed active sites, and at this lowest SR ions have more time to intercalate into the material's channels. These interpretations support the overall capacitive and diffusive behaviour. Based on these explanations, the specific

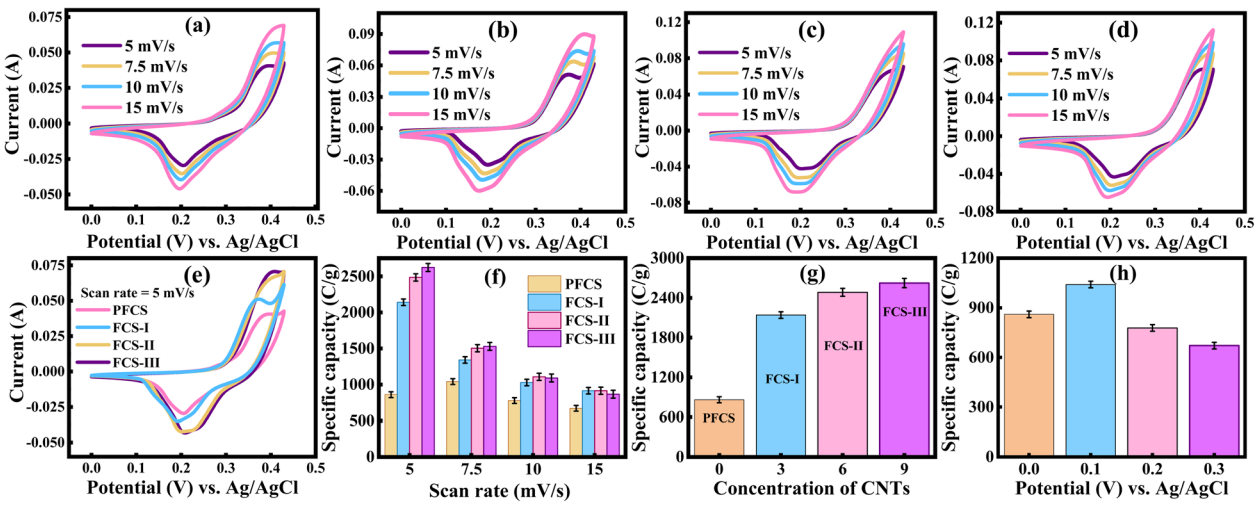

Fig. 6 (a–d) CV curves of PFCS, FCS-I, FCS-II, and FCS-III, (e) combined plot at 5 mV s^{-1}, (f) scan rate *vs.* specific capacity, (g) CNTs concentration *versus* specific capacity, and (h) potential *versus* specific capacity.

Table 2 Specific capacities of PFCS, FCS-I, FCS-II, and FCS-III at different scan rates

	Specific capacities (C g^{-1})			
Scan rate (mV s^{-1})	PFCS	FCS-I	FCS-II	FCS-III
5	860.55	2141.15	2485.33	2624.16
7.5	1040.99	1341.67	1504.07	1529.19
10	778.22	1028.95	1106.95	1091.03
15	671.13	914.26	913.77	866.75

capacity (Q_s) was calculated using eqn (3) for all prepared samples. The rationale behind the computation of Q_s is the matching of the ideally reported battery-type SC profile, which is what the several reports have presented.[31,36,38]

$$Q_s = \frac{\int_{V_i}^{V_f} I\,dV}{mv} \quad (3)$$

Here, Q_s refers to specific capacity in C g^{-1}, and the integral term in this expression denotes the area under the CVs, while m and v are associated with active mass and SR, respectively.

The Q_s values of PFCS, FCS-I, FCS-II, and FCS-III are listed in Table 2 at various SRs (5–15 mV s^{-1}). It is clear that a remarkable Q_s of 2624 C g^{-1} was calculated for the FCS-III electrode material, surpassing previously reported PFCS-based composites. This also highlights the effective integration of CNTs into the ternary TMS-based material. However, a gradual decrease in Q_s values is observed with increasing SR, indicating sluggish ion migration into the electrode channels due to limited ion diffusion time at higher SR. Conversely, higher Q_s values at low SR are due to most active sites being occupied by ions, thanks to the longer diffusion time. Additionally, the influence of CNT concentration on Q_s values is evident, as illustrated in Fig. 6(f). Consequently, the FCS-III electrode material, which has maximum CNT contents, achieved an ultra-high Q_s among the electrode materials, as can be seen in Fig. 6(g). Also, a gradual increment in CNT content causes the systematic reduction in the ΔE_p, as shown in bar graph Fig. 6(h), plotted ΔE_p *versus* concentration of CNTs at the lowest SR (~5 mV s^{-1}). This progressive reduction in ΔE_p values indicate faster electrode kinetics, more reversibility, and charge transfer efficiency of FCS-based electrode materials.

To better understand the charge storage behaviour of the synthesized PFCS-based electrode materials, Dunn's method has been used. This theoretical approach helps to clarify how charge carriers are stored in PFCS, FCS-I, FCS-II, and FCS-III. More importantly, the quantitative separation of storage processes, such as surface-controlled and diffusion-controlled mechanisms, has been estimated, which accounts for the total storage capacity. For this purpose, Dunn and his co-workers applied power's law, which is expressed in eqn (4).

$$i_{peak} = av^b \text{ or } \log(i_{peak}) = b\log(v) + \log(a) \quad (4)$$

Herein, i_{peak} clarifies the oxidation and reduction peak currents from CVs. Specifically, a and b are considered fitting parameters that depend on the SR, and they are associated with the slope and intercept obtained from the linear fitting of SR *versus* peak current plots. From this, the average value of b can be determined, and when it equals 0.5, it indicates completely diffusion-controlled behavior. This reflects a traditionally typical battery-type phenomenon, meaning ions are diffusing into the tunnels of the electrode material. On the other hand, a b-value of 1 represents surface-controlled phenomena. This condition includes both capacitive and pseudocapacitive (surface redox-activity) processes, suggesting double-layer formation and rapid surface-redox reactions occurring at or near the electrode's surface. More importantly if b-value is close to 0.5, it indicates the dominance of battery-type behavior. Conversely, if b is near 1, surface-controlled behavior is more prevalent. So, the combination of capacitive and diffusive behaviors, which contribute to the overall storage capacity, therefore, these conditions collectively indicate battery-type behavior of the

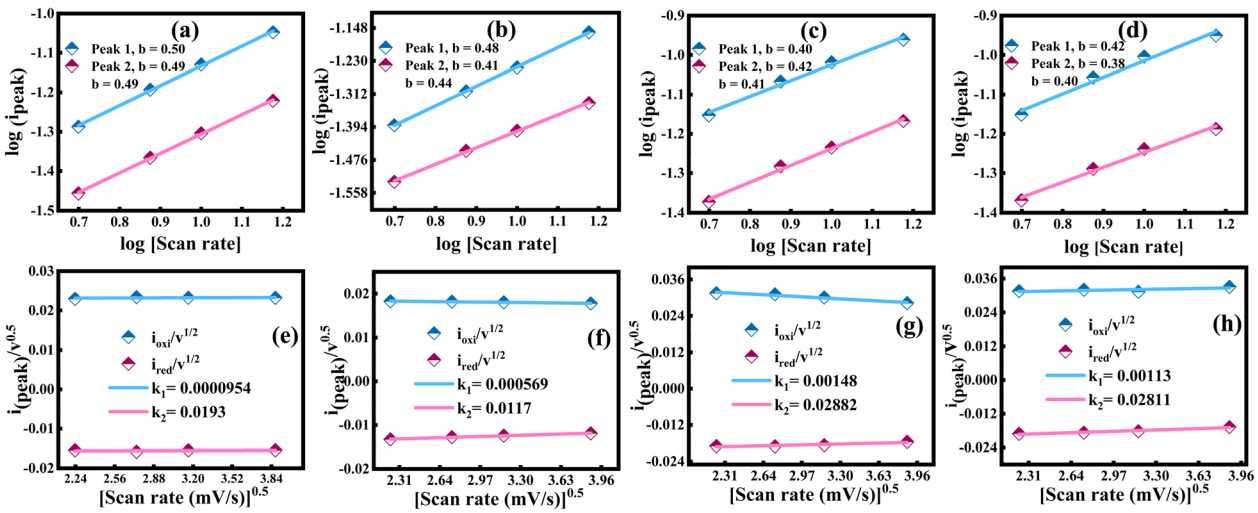

Fig. 7 (a–d) Linearly fitted graphs for all samples and (e–h) contribution parameters (k_1, k_2) for all samples.

electrode material. Therefore, Fig. 7(a–d) shows the graphs of *b*-values calculated for PFCS, FCS-I, FCS-II, and FCS-III, which are 0.49, 0.44, 0.41, and 0.40, respectively, confirming battery-type behavior. These values indicate the coexistence of capacitive and diffusive processes and clarify the presence of redox-active sites due to sulfur vacancies and additional functional groups in the surface chemistry of as-fabricated electrodes, which are associated with pseudocapacitive behavior and partial chemically inert surface-active sites belonging to non-pseudocapacitive behavior (EDLC). These contributions showed some alterations when functionalized CNTs were decorated on the surface chemistry of PFCS. That's how the battery-type behaviors in all fabricated electrodes were observed and reported after careful comparison with different reports from the literature.[34–37]

Furthermore, in the context of quantifying surface-controlled and diffusion-controlled contributions individually at various SR for all prepared PFCS-based electrode materials, the Dunn method was employed. This method has been quantified into eqn (5) and (6).

$$i_{peak} = k_1 v + k_2 v^{1/2} \quad (5)$$

This equation refers the current from surface-controlled ($k_1 v$) and diffusion-controlled ($k_2 v^{1/2}$) process, and is quantified for linear fitting,

$$\frac{i_{peak}}{v^{1/2}} = k_1 v^{1/2} + k_2 \quad (6)$$

The graph $v^{1/2}$ *vs.* $i_{peak}/v^{1/2}$ were plotted for each PFCS-based electrode materials, as depicted in Fig. 7(e–h).

By the fitting of these plots, the obtained slope and intercepts yield the values of k_1 and k_2 constants, and were then used to compute relative contributions at various SR. Fig. 8(a–d) demonstrates the deconvoluted plots of surface-controlled and diffusion-controlled phenomenon of PFCS, FCS-I, FCS-II, and FCS-III at various SR (5–15 mV s^{-1}). It can be observed in contribution ratios' graphs that PFCS is exhibiting dominantly diffusion-controlled phenomenon, which is consistent with its *b*-value (0.49). A transition from slow diffusion-controlled to more ideal battery-type phenomenon can be clearly observable in Fig. 8(a–d) for 3 (FCS-I), 6 (FCS-II), and 9% CNTs (FCS-III). The rationale behind this transition is the shortening of diffusion distances and conductive scaffold provided by the incorporated CNTs content into PFCS, allowing the faster kinetics. Additionally, a sharp rise in surface-controlled phenomenon can be noticed with the elevation in SR for all prepared samples. The decrease in diffusion-controlled phenomenon is likely due to insufficient time availability of ions to diffuse into the PFCS-based electrode materials at elevated SR. Such theoretical predictions support the battery-type behavior of FCS-III and confirm their suitability for next-generation HCs technology. The contribution of these behaviors (capacitive and diffusive) directly originating from the CV curves at lowest SR are displayed in Fig. 8(e–h), representing the PFCS, FCS-I, FCS-II, and FCS-III, respectively.[34,38]

To evaluate a comprehensive view of hybrid performance for PFCS-based electrode materials, GCD analysis was conducted over various current densities of 10, 13, 16, and 20 A g^{-1} within an optimized potential range of 0–0.45 V. The obtained curves depicted in Fig. 9(a–d) confirmed a battery-type behavior for all PFCS-based composites, which aligns with the CV analysis. The GCD curves also maintained symmetrical shapes even at elevated current density (~20 A g^{-1}), suggesting significant stability, cyclability, and kinetic robustness of these electrodes. This smooth charge storage phenomenon validates their suitability for SC applications. Furthermore, the fabricated electrodes experienced a reduction in charging and discharging times along with increased potential drops as the current density is elevated from 10 to 20 A g^{-1}, as can be noticed in Fig. 9(a–d). The charging and discharging times of the electrodes are influenced by the varying content of CNTs. With the addition of different percentages of CNTs into PFCS, optimized electrochemical performances were achieved synergistically, as illustrated in Fig. 9(a–d). This phenomenon indicates that the incorporated CNTs have led to increased discharge cycles due to

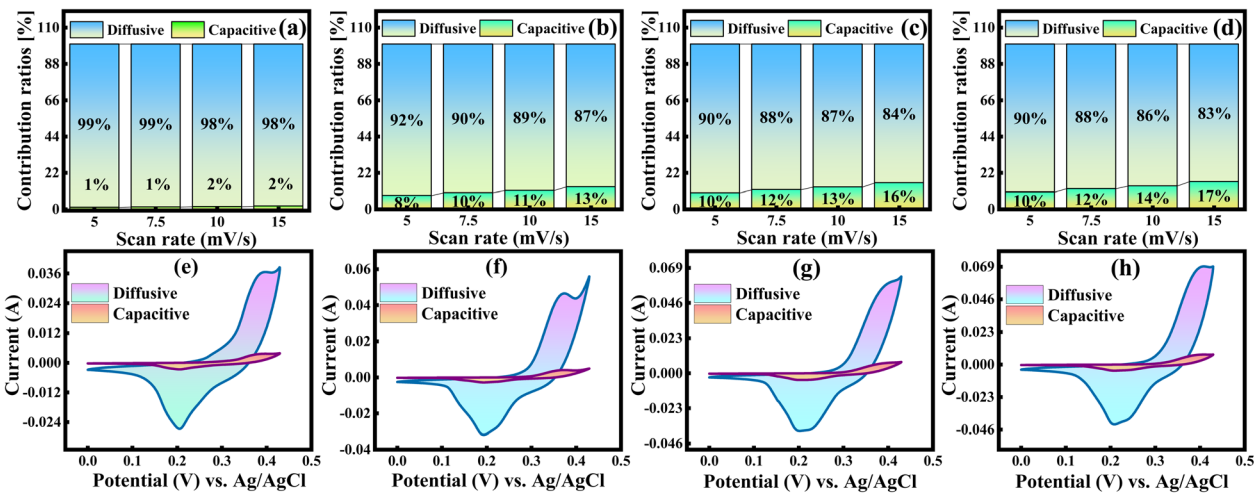

Fig. 8 (a–d) Contribution graphs for all samples and (e–h) capacitive and diffusive contributions in CV curves at 5 m V s^{-1} for all samples.

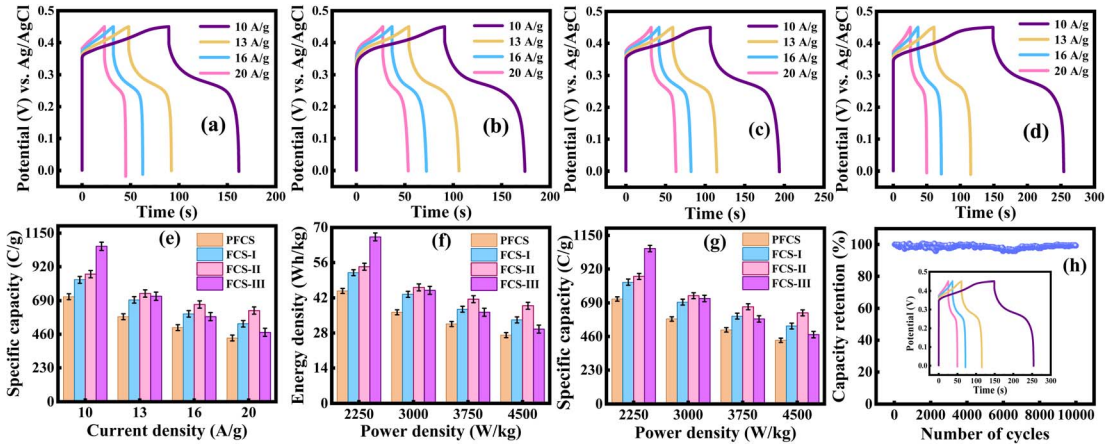

Fig. 9 GCD profiles (a) PFCS, (b) FCS-I, (c) FCS-II, (d) FCS-III, (e) current density *vs.* specific capacity, (f) Ragone plot, (g) power density *vs.* specific capacity, and (h) stability test.

enhanced ionic mobility and a reduction in potential drop (*iR* drop). With the incorporation of CNTs content, the *iR* drop at the lowest I_m (~10 A g^{-1}). The *iR* drop is responsible for the voltage loss during electrochemical reaction due to the internal resistance of any electrochemical system. Thus, the lowest *iR* drop for FCS-III (9% CNTs) suggests an effective strategy for mitigating the internal resistances of PFCS-based electrode materials. Also, at low current densities, the faradaic process is more effectively facilitated thanks to the maximum available time for electrolyte species to intercalate into the exposed active sites of PFCS-based electrode materials. Thus, the Q_s was computed using eqn (7).

$$Q_s = I_m \times \Delta t \quad (7)$$

where I_m represents the current density (A g^{-1}) while Δt expresses discharging time for electrode materials. The Q_s of 716, 831, 869, and 1059 C g^{-1} were acquired at 10 A g^{-1}, including PFCS, FCS-I, FCS-II, and FCS-III electrode materials.

In the case of FCS-based electrode materials, the FCS-III electrode exhibited superior Q_s due to its advantageous web-like morphology. Additionally, Fig. 9(e) illustrates a graph showing the relationship between Q_s and I_m for all prepared samples. This graph indicates a gradual decrease in Q_s as I_m increases. It also highlights the effects of CNTs' concentration and I_m on the charge-storage capabilities of the fabricated electrode materials. Notably, the PFCS shown in Fig. 9(e) achieved the maximum Q_s of 716 C g^{-1} at I_m equal to 10 A g^{-1}, which substantially decreased to 386 C g^{-1} at 20 A g^{-1}. Similarly, a parallel trend was observed for the sample with 3% CNTs (FCS-I), where the storage capacity of about 831 C g^{-1} at 10 A g^{-1} dropped to approximately 513 C g^{-1} at 20 A g^{-1}. Furthermore, adding 6% and 9% CNTs into PFCS increased this Q_s to 869 and 1059 C g^{-1} at 10 A g^{-1} for FCS-II and FCS-III, respectively, but it decreased significantly at higher I_m. This reduction in capacity is due to less time available for ions to migrate into the electrode's pores and active sites, as shown clearly in the FESEM images in Fig. 4(a–d). Furthermore, the Q_s values for all samples at all current densities have been reported in different conversion units, aiming to provide a comprehensive quantitative overview in Table 3. The rationales behind these significant improvements are a highly porous nickel foam substrate and a stable contact between the electrode/electrolyte interface. At low current densities, these values are within the expected range, reflecting efficient ion diffusion due to the proper response of electrolyte ions to the applied electrical signal. These achievements reflect our optimized electrochemical testing, in which the active mass loading was ensured across multiple experiments under the same and different conditions. Whereas the ED and PD for all PFCS-based samples are listed in the Table 4 and were calculated using eqn (8) and (9).

$$\mathrm{ED} = \frac{\Delta V \times Q_s}{2 \times 3.6} \quad (8)$$

$$\mathrm{PD} = \frac{\mathrm{ED} \times 3600}{\Delta t} \quad (9)$$

These are standard equations used to estimate precise performance metrics like ED and PD of as-synthesized electrodes. Compared to other prepared samples, the FCS-III achieved the maximum ED of 66.22 Wh kg^{-1} along with a notable PD of 2250 W kg^{-1} at 10 A g^{-1}. These impressive metrics are summarized in Table 4 alongside reported literature. Furthermore, these performance metrics are plotted against various I_m (Ragone plot), which further highlights the behavior of all samples, observable in Fig. 9(f). In this context, the Ragone plot shows that an increase in ED often results in a decrease in PD, or *vice versa*, because fewer ions are available for delivery. Additionally, Fig. 9(g) illustrates the trend of PD with Q_s, showing how varying the concentration of CNTs affects the ED values of all samples. Alongside these advantageous charge-storage traits, the stability of FCS-III was evaluated by establishing an asymmetric setup in which FCS-III served as the cathode and activated carbon as the anode, with 10 000 GCD cycles, yielding 98.76% charge storage retention, as depicted in

Table 3 Conversions of specific capacities of PFCS, FCS-I, FCS-II, and FCS-III into different units

Sample	Mass loading (mg cm^{-2})	Current density (A g^{-1})	Specific capacitance (F g^{-1})	Specific capacity (C g^{-1})	Specific capacity (mAh g^{-1})	Areal capacity (C cm^{-2})
PFCS	1.5	10	1592.56	716.65	199.07	1.074
	1.5	13.34	1288.94	580.02	161.11	0.870
	1.5	16.67	1122.89	505.30	140.36	0.757
	1.5	20	964.43	433.99	120.55	0.650
FCS-I	1.5	10	1846.78	831.05	230.84	1.246
	1.5	13.34	1544.30	694.93	193.03	1.042
	1.5	16.67	1331.88	599.35	166.48	0.899
	1.5	20	1181.03	531.46	147.62	0.797
FCS-II	1.5	10	1931.14	869.01	241.39	1.303
	1.5	13.34	1642.26	739.01	205.28	1.108
	1.5	16.67	1474.59	663.56	184.32	0.995
	1.5	20	1382.17	621.97	172.77	0.932
FCS-III	1.5	10	2354.71	1059.62	294.33	1.589
	1.5	13.34	1600.54	720.24	200.06	1.080
	1.5	16.67	1289.87	580.44	161.23	0.870
	1.5	20	1050.56	472.75	131.32	0.709

Table 4 Specific capacity, energy density, and power density of PFCS, FCS-I, FCS-II, and FCS-III at multiple current densities

Sample	Current density (A g^{-1})	Specific capacitance (F g^{-1})	Specific capacity (C g^{-1})	Energy density (Wh kg^{-1})	Power density (W kg^{-1})
PFCS	10	1592.56	716.65	44.79	2250
	13.34	1288.94	580.02	36.25	3000
	16.67	1122.89	505.30	31.58	3750
	20	964.43	433.99	27.12	4500
FCS-I	10	1846.78	831.05	51.94	2250
	13.34	1544.30	694.93	43.43	3000
	16.67	1331.88	599.35	37.45	3750
	20	1181.03	531.46	33.21	4500
FCS-II	10	1931.14	869.01	54.31	2250
	13.34	1642.26	739.01	46.18	3000
	16.67	1474.59	663.56	41.47	3750
	20	1382.17	621.97	38.87	4500
FCS-III	10	2354.71	1059.62	66.22	2250
	13.34	1600.54	720.24	45.01	3000
	16.67	1289.87	580.44	36.27	3750
	20	1050.56	472.75	29.54	4500

Table 5 Comparison of performance parameters of different electrode materials

Sample	Specific capacitance (F g^{-1})	Energy density (Wh kg^{-1})	Power density (W kg^{-1})	Cyclic stability (%)	References
$FeCo_2S_4$@MXene	2415.3	68	800	90.50% after 5k cycles	19
$FeCo_2S_4$/MWCNTs	432	49.40	20k	93.9% after 5k cycles	26
$FeCo_2S_4$@Ni@graphene	390 mAh g^{-1}	65.8	754.8	89% after 6k cycles	27
$FeCo_2S_4$/NF	4035	37.7	603	80.40% after 5k cycles	32
$FeCo_2S_4$/rGO/Ag/NF	1840	59	817	94% after 10k cycles	33
$FeCo_2S_4$/CNTs	1059.62 C g^{-1}	66.22	2250	98.76% after 10k cycles	This work

Fig. 9(h). The supporting literature has been reported in Table 5.[19,26,27,32,33]

The EIS analysis tests were conducted within an optimized frequency range from 10^{-2} to 10^{4} Hz to gain a more comprehensive understanding of electrochemical responses such as ionic mobility, diffusion dynamics, and ion transport in all samples. In this context, circuit elements such as solution resistance (R_s), R_{ct}, and Warburg impedance (W) are fundamental parameters. These parameters help us to examine the influence of varying CNT concentration more deeply. In this regard, the Nyquist plot is displayed in Fig. 10(a), where the real and imaginary impedances are represented on the x and y-axes,

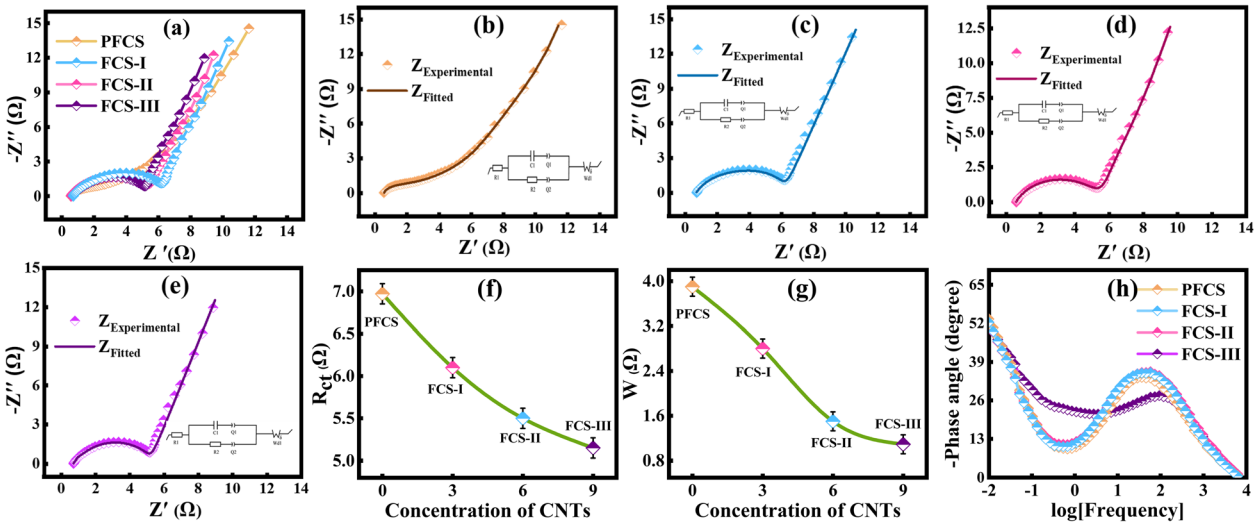

Fig. 10 (a) Combined EIS spectra of all samples, (b–e) fitting spectra of PFCS, FCS-I, FCS-II, and FCS-III, (f) concentration of CNTs *vs.* charge transfer resistance, (g) concentration of CNTs *vs.* Warburg resistance, and (h) Bode plot.

respectively. This Nyquist plot shows the EIS spectra of PFCS, FCS-I, FCS-II, and FCS-III. In these spectra, dynamic changes in capacitive and resistive parameters can be observed with varying CNT concentrations. To better interpret this behavior, the Nyquist plot is divided into high, intermediate, and low-frequency regions. These regions demonstrate the circuit elements mentioned earlier, such as R_s, R_{ct}, and W, which are useful for optimizing the electrochemical response of electrode materials for SC technology.

Within this framework, the Biologic EC Lab V11.60 software, using the well-suited Randle circuit, was employed to evaluate the exact values of the circuit elements for all PFCS-based electrodes, as displayed in Fig. 10(b–e). For all samples, the fitted and experimental data are separated by two distinctive legends, indicating a well-matched equivalent circuit with real measurements. Consequently, all the PFCS-based composites with CNTs (PFCS, FCS-I, FCS-II, and FCS-III) exhibit R_s (0.59, 0.53, 0.60, and 0.55 Ω), R_{ct} (6.97, 6.10, 5.50, and 5.15 Ω), and W (3.9, 2.8, 1.50, and 1.09 Ω), as listed in the Table 6. Nonetheless, the balanced R_s values in the high-frequency region suggest optimal ionic conductivity (σ) for all samples. More importantly, the R_{ct} in the intermediate-frequency region helps quantify the resistance barrier during electron transfer and reveals how easily or difficult it is for a redox reaction to occur at interface of the electrode and electrolyte. The R_{ct} can also be calculated by subtracting R_s from the width of the semicircle on a Nyquist plot, shown in Fig. 10(a). As a result, the R_{ct} values and the width of the semicircle gradually decrease with the incorporation of CNT content, as can be seen in Fig. 10(f). This low R_{ct} values signifies the importance of CNT addition, further indicating faster electron transfer which is critical for enhancing the electrochemical response of electrode materials.

Moreover, the line growing vertically in the low-frequency region, just after the semicircle, is associated with W and diffusion dynamics, as shown in Fig. 10(a). The significant reduction in W values from 3.9 to 1.09 Ω with the gradual addition of CNTs, as shown in Fig. 10(g), indicates excellent diffusion of ionic species through the electrode–electrolyte interface. Additionally, it can be inferred that ionic species rapidly fill the vacancies created by quick electron transfer due to low R_{ct}, leading to improved ion transport and diffusion dynamics. Notably, the W value decreased significantly with the highest CNTs' content in PFCS and shifted toward the y-axis, as clearly be seen in Fig. 10(a). This shift confirms the transition toward capacitive-dominated behavior of FCS-III by enhancing its diffusion-limited characteristic. These low R_{ct} and W values, as listed in Table 6, highlight the efficient electrochemical response of FCS-III, making it a superior electrode material for advanced SCs.

The electrochemical kinetics and storage mechanism dynamics of PFCS, FCS-I, FCS-II, and FCS-III were analyzed using Bode analysis, as shown in Fig. 10(h). This plot illustrates the frequency-dependent characteristics of all samples against phase angle (θ), showing how the impedance of the SC shifts between ideal capacitive ($\theta = -90°$) and pure resistive ($\theta = 0°$) behaviors at very low and high frequencies, respectively. When the resistive and capacitive impedances are considered to be equally contribution at $\theta = -45°$, known as the knee frequency (f), it is an important metric for evaluating the relaxation time constant (τ). This τ indicates the minimum timescale required

Table 6 Values of elements for the corresponding fit circuit. $R_1 = R_s$, $R_2 = R_{ct}$, C_1 = capacitance, Q_1, Q_2 = constant phase elements, and W_1 = Warburg impedance

Sample	R_1 (Ω)	R_2 (Ω)	C_1 (mF)	Q_1 (F $s^{(a-1)}$)	Q_2 (F $s^{(a-1)}$)	W_1 (Ω)
PFCS	0.63	6.99	0.032	0.217	0.0023	3.9
FCS-I	0.53	6.16	0.011	0.0082	0.619	2.8
FCS-II	0.60	5.13	0.015	0.011	0.716	2.05
FCS-III	0.55	4.41	0.056	0.035	0.077	1.39

for an SC device to discharge all stored energy efficiently at constant power. Crucially, lower τ values suggest better rate performance of the SC device. Therefore, τ is calculated as the inverse of for all samples, using eqn (10).

$$\tau = \frac{1}{f} \tag{10}$$

Herein, τ for PFCS, FCS-I, FCS-II, and FCS-III were computed to be 27, 17, 16, and 10 ms, respectively. Such a systematic decrease in τ values is attributed to the inclusion of CNTs, which manifests excellent rate capability in the FCS-III electrode material for advanced SC technology.

The σ of the electrolyte immediately estimates the electrochemical efficiency of electrode materials for SCs based on their ion-conduction capability. For comparison, this fundamental property is crucial for assessing the ease with which charge carriers flow during charging and discharging within the electrolyte. To evaluate this, the R_s of all prepared samples are measured using EIS with the help of EC Lab software, an important factor in calculating σ (S cm^{-1}). Eqn (11) has been used to determine the σ values of each electrode material.[30–37]

$$\sigma = \frac{L}{A \times R_i} \tag{11}$$

In this equation, L and A relate to the thickness (0.09 cm) and cross-sectional area (1.0 cm^2) of the electrode material being dipped into the electrolyte. The symbol R_i signifies the solution resistance to charge carriers at the electrode surface and the reference electrode in an electrolyte (KOH). The ionic conductivities for PFCS, FCS-I, FCS-II, and FCS-III were calculated to be 0.152, 0.169, 0.150, and 0.163 S cm^{-1}, respectively. These consistent values indicate stable σ across all samples, even with the addition of CNTs, suggesting no disruption to ionic pathways and indicating gradual improvements in ionic conduction. It can be concluded that incorporating CNTs enhances electronic and ionic conductivity while maintaining stable σ values. Therefore, FCS-based electrode materials exhibit excellent electrochemical efficiency, confirming their suitability for SC applications.

The cation transference number (t_+) is another important parameter for evaluating the fraction of the total ionic current carried by cations (K^+, OH^-) in a 1 M KOH electrolyte. Specifically, this parameter indicates which ion migrates more efficiently. It is important to note that an equal distribution of ionic current is not possible due to factors such as the size of solvated ions, electrostatic polarization interactions, and temperature, which all influence an ionic species' migration efficiency relative to others. In this context, t_+ values for PFCS, FCS-I, FCS-II, and FCS-III electrode materials have been estimated using the following eqn (12), proposed by Sorenson & Jacobsen.[30,34]

$$t_+ = \frac{1}{1 + Z_d(0)/R_b} \tag{12}$$

Here, $Z_d(0)$ demonstrates the Warburg impedance's real part at approximately 0 Hz, and R_b represents solution resistance. Our findings show that t_+ values increased significantly from 0.13, 0.15, 0.22, and 0.28 for PFCS, FCS-I, FCS-II, and FCS-III, indicating a strong shift toward leading ion migration. Additionally, the very small t_+ value of PFCS highlights a diffusion-limited mechanism for K^+ ions due to its bulk form, resulting in anion (OH^-) dominated kinetics. A gradual increase in t_+ values is clearly observable, which is attributed to the addition of CNTs into the parent material. The incorporation of CNTs enhances cation mobility and promotes a balanced contribution of both ions (K^+, OH^-) in the charge storage process by reducing the kinetic limitations of the parent material, thanks to the conductive scaffold provided by CNTs. It is important to note that this ionic participation significantly helps in reducing the polarization at higher SR. Furthermore, the increased cation mobility substantially improves storage efficiency, thereby enhancing the intercalation of K^+ ions into the FCS-III electrode during faradaic reactions.

The rate constant indicates how quickly a reaction occurs and provides an estimate of electron transfer between the electrode and electrolyte ions during a redox reaction. It is a kinetic parameter closely related to charge-transfer resistance. A high rate constant indicates a fast redox reaction, resulting in greater charge storage, higher power, and better performance. The rate constant is calculated using eqn (13).[30,36]

$$\text{Rate constant} = \frac{RT}{F^2 \times R_{ct} \times C} \tag{13}$$

Here, R and T in the numerator represent the gas constant and room temperature, while parameters in the denominator, such as F, R_{ct}, and C, are related to the Faraday constant, charge transfer resistance calculated from EIS analysis, and electrolyte concentration, respectively. Within this context, the values of the rate constant for each fabricated electrode are 3.80×10^{-8}, 4.32×10^{-8}, 5.18×10^{-8}, and 6.03×10^{-8} cm s^{-1}, respectively.

Exchange current density is a crucial parameter in electrochemistry, indicating how readily charge-transfer reactions occur at the electrode–electrolyte interface at equilibrium (when no current flows). It represents the rate at which electrons are exchanged between the electrode and ions in the electrolyte at the equilibrium potential. A high exchange current density signifies rapid reaction kinetics and a lower overpotential to drive current. This can be evaluated using eqn (14).[29,30,36]

$$J_0 = \frac{RT}{n \times F \times R_{ct}} \tag{14}$$

The quantitatively estimated values are 1.83, 4.16, 5.01, and 5.82 mA g^{-1}, respectively. This indicates the highest exchange current density for FMO-III (5.82 mA g^{-1}), providing additional evidence that it truly exhibited excellent ion transport characteristics compared to all other materials in the as-fabricated electrode series.

Discussing cation mobility in electrochemistry is vital for understanding how ions move within an electrochemical cell, which directly impacts the system's performance. This property reveals how easily positive ions, or cations, can move through an electrolyte against an applied electrical signal to maintain

neutrality, thereby suppressing polarization effects. For example, high cation mobility allows ions to move quickly and store charge, resulting in greater energy storage capacity in a cell. This characteristic varies among different electrolytes and systems, with common electrolytes like KOH and NaOH chosen for their low cost, minimal side effects, and anti-corrosive properties. A key factor affecting the system's efficiency is the size of the solvated ionic radii, typically defined as the ratio of charge to volume for a cation. Therefore, cations with smaller hydrated radii are preferred because they have lower solvent shell energy, enabling them to diffuse more easily within the electrolyte. In this context, cation mobility in KOH is described by eqn (15).[36]

$$u_+ = \frac{t_+ \times \sigma}{n \times z^2 \times e} \quad (15)$$

In the above equation, t_+ and σ are the transference number of the cation and ionic conductivity, respectively. Meanwhile, n, z^2, and e are parameters known as number density, charge number, and elementary charge. The quantitative examination of cation mobility for PFCS, FCS-I, FCS-II, and FCS-III yields values approximately 2.03×0^{-10}, 2.65×0^{-10}, 2.81×0^{-10}, and 3.81×0^{-10} m^2 V^{-1} s^{-1}, respectively, expressing the highest cation mobility for FCS-III.

Extending the earlier-discussed electrochemical investigations, an in-depth study of the FCS-III//AC device has been systematically conducted using CV, GCD, and EIS characterizations with 1 M KOH electrolyte. A charge storage setup is illustrated in Fig. 11, in support of its application perspective. Particularly, in CV analysis, as depicted in Fig. 12(a), the absence of significant distortions in the obtained symmetrical CVs, along with redox humps at SR ranging from 50 to 500 mV s^{-1}, suggests excellent stability and a hybrid (PC and EDLC) nature of this assembled device. Also, remarkable reversibility for FCS-III//AC is observed across variable potential windows (0–1.2 V). This reversibility is reflected in a gradual increase in CV area while maintaining symmetry, as clearly seen in Fig. 12(b). The rationale behind these stable electrochemical features is attributed to smooth contact at the electrode/electrolyte interface and efficient electrode kinetics, thereby promoting the effectiveness of the FCS-III//AC device.[36,38]

GCD tests were carried out to precisely estimate the performance metrics at various current densities, ranging from 1.5 to 9 A g^{-1}, within the same potential window, consistent with CV analysis. The obtained nonlinear and consistent GCD curves confirm good rate capability and indicate dominant faradaic contributions from the FCS-III positive electrode, as illustrated in Fig. 12(c). Additionally, this hybrid device delivers the longest discharge time at the minimum current density of 1.5 A g^{-1}, signifying the impact of the electrode matrix that utilizes redox-active sites effectively. However, at elevated current densities, the discharge period shrinks systematically, mainly due to limited ion intercalation and increased polarization from Helmholtz layer formation at the electrode surface at higher rates. Notably, the positive electrode (FCS-III) promotes swift reversible redox activity, and the negative electrode (AC) facilitates fast charge delivery even at higher current densities.[38] This synergistic configuration also minimizes internal resistances by reducing the *iR* drop, as portrayed in Fig. 12(c), further promoting efficient charge transport in electrode channels. Overall, these traits validate this FCS-III//AC configuration for optimizing pseudocapacitive-type storage and capacitive rate

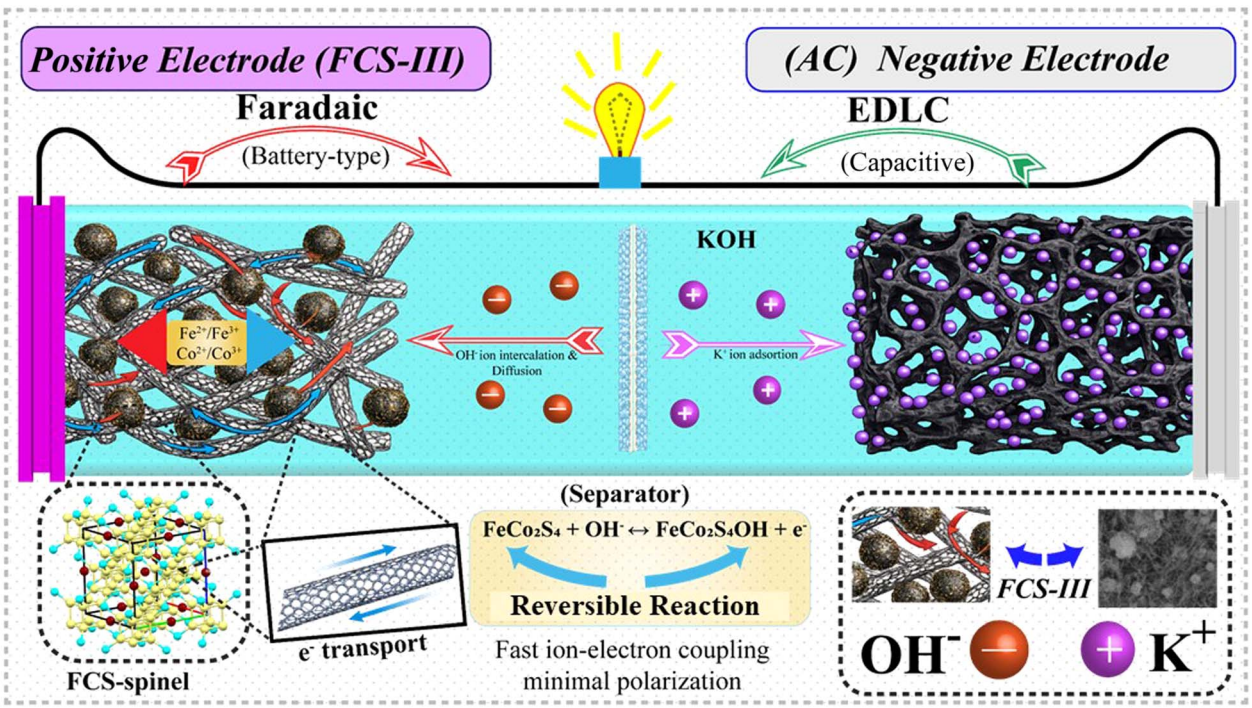

Fig. 11 Pictorial representation of charge storage mechanism.

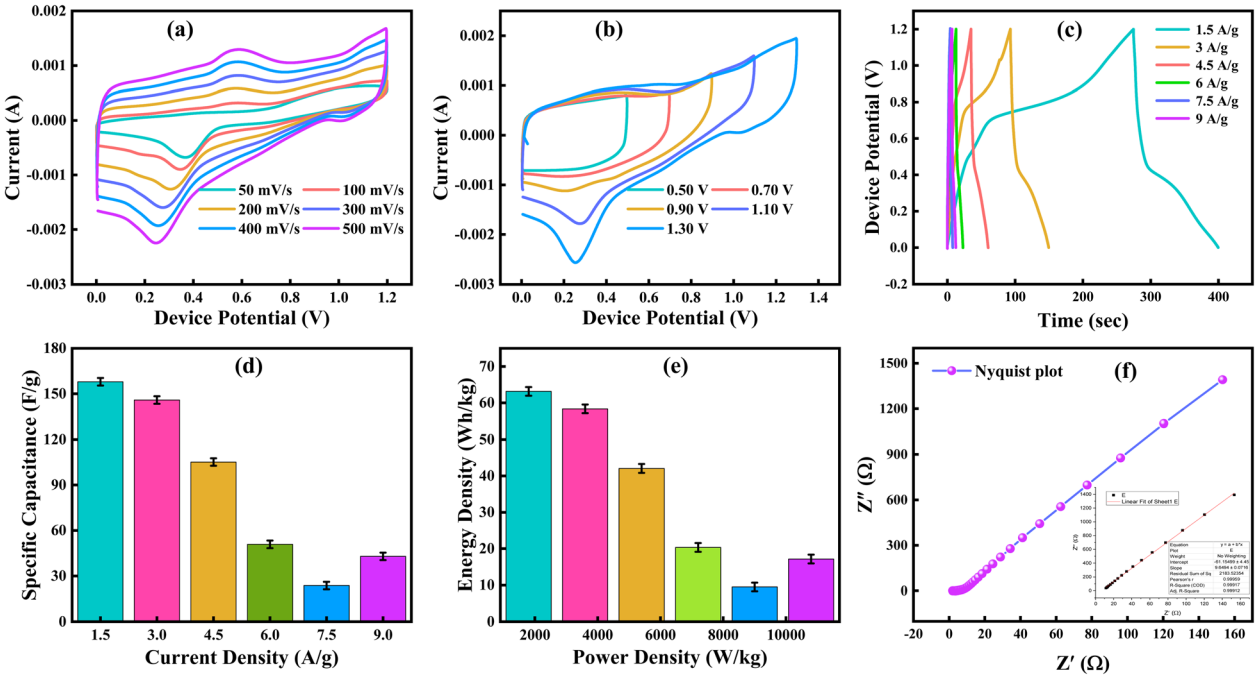

Fig. 12 (a and b) CV curves of FCS-III//AC at 1.2 V and at different potential windows, (c) GCD profiles at multiple current densities, (d) current density *vs.* specific capacitance, (e) Ragone plot, and (f) Nyquist plot.

performance, showing its suitability for SC applications.[36,38,39] The quantification of this charge storage type has been done with the help of the stated eqn (16)–(18).[38]

$$C_{sp} = \frac{I \times \Delta t}{m \times \Delta V} \quad (16)$$

$$ED = \frac{\Delta V^2 \times C_{sp}}{3.6} \quad (17)$$

$$PD = \frac{ED \times 3600}{\Delta t} \quad (18)$$

Additionally, the trend of C_{sp} as a function of current density is shown in Fig. 12(d), indicating a gradual decrease in charge storage with increasing current density. This fact is associated with the inefficient response of the applied electrical signal towards the electrolyte ions, which limits their diffusion time. Therefore, at 1.5 A g^{-1}, the constructed device facilitated the highest capacitance of 157.88 F g^{-1} and 42.90 F g^{-1} at 9 A g^{-1}. A similar trend has been observed in the Ragone plot, corresponding to the PD *versus* ED trend, as supplemented in Fig. 12(e). At this instance, the maximum ED and PD values were 63.15 Wh kg^{-1} and 10 800 W kg^{-1}, respectively. The rest of the values are provided in Table 7.

To evaluate comprehensive insights into the electrochemical response of the FCS-III//AC device, including charge transport and diffusion dynamics, EIS is employed across a wide range of frequencies. The EIS spectra, as depicted in Fig. 12(f), are categorized into three effective regions; (i) the high-frequency region describes R_s, (ii) the intermediate region demonstrates R_{ct}, and (iii) the third region represents W_d. More importantly, these elements exhibit the interfacial characteristics of the electrode in a given solution. R_s, R_{ct}, and W_d are simulated using EC Lab software to estimate them accurately, where the line represents simulated data and the solid spheres indicate experimental impedances. From the simulation, extremely small impedance values, such as R_s (1.96 Ω), R_{ct} (1.39 Ω), and W_d

Table 7 Performance parameters of FCS-III//AC based asymmetric device

Current density (A g^{-1})	Discharge time (s)	Potential window (V)	Specific capacitance (F g^{-1})	Energy density (Wh kg^{-1})	Power density (Wh kg^{-1})
1.5	126.31	1.2	157.88	63.15	1800
3.0	58.36	1.2	145.90	58.36	3600
4.5	28.04	1.2	105.15	42.06	5400
6.0	10.17	1.2	50.85	20.34	7200
7.5	3.79	1.2	23.88	9.47	9000
9.0	5.72	1.2	42.90	17.16	10 800

(9.64 Ω), were obtained, suggesting swift electrode kinetics in FCS//AC.

4. Conclusion

In summary, we synthesized $FeCo_2S_4$ and its composites with different CNTs compositions (3%, 6%, and 9%) using hydrothermal and solvothermal methods. Various analysis techniques, including XRD, EDX, and SEM, were used to confirm that all samples had a crystalline structure with a simple cubic phase. The successful incorporation of CNTs into the PFCS structure was validated by EDX analysis, while morphological analysis revealed well-defined grains with a non-uniform distribution. To evaluate the EC, a three-electrode system was employed. Among the fabricated electrodes, the FCS-III composite showed the best performance, delivering a specific capacity of 1059.62 C g^{-1}, an energy density of 66.22 Wh kg^{-1}, and a power density of 2250 W kg^{-1} at 10 A g^{-1}. Additionally, the electrode demonstrated excellent cycling durability, retaining 98.76% of its capacity after 10 000 cycles and maintaining a stable coulombic efficiency. EIS results indicated that the prepared material exhibited good electrical performance, with low charge transfer resistance (4.41 Ω), improved ionic conductivity (0.13 S cm^{-1}), and a short relaxation time (0.010 s). The incorporation of 9% CNTs into FCS enhanced its potential as an excellent electrode material for advanced supercapacitor applications.

Conflicts of interest

The authors declare that there are no financial or any other types of conflicts of interests to declare for this submission.

Data availability

Data will be made available on request.

Acknowledgements

The authors would like to acknowledge Ongoing Research Funding Program, (ORF-2026-71), King Saud University, Riyadh, Saudi Arabia.

References

1 H. Kaur, A. Thakur, R. C. Thakur and A. Kumar, A review on the multifaceted role of ionic liquids in modern energy storage systems: from electrochemical performance to environmental sustainability, *Energy Fuels*, 2025, **39**(8), 3703–3734.
2 A. Asghar, K. Khan, M. S. Rashid, M. Hamza, Z. Liu, C. Liu, *et al.*, Extrusion-based additive manufacturing of carbonaceous and non-carbonaceous electrode materials for electrochemical energy storage devices, *Adv. Mater. Technol.*, 2025, **10**(3), 2400136.
3 Y. Wang, J. Xiao, T. Zhang, L. Ouyang and S. Yuan, Single-step preparation of ultrasmall iron oxide-embedded carbon nanotubes on carbon cloth with excellent superhydrophilicity and enhanced supercapacitor performance, *ACS Appl. Mater. Interfaces*, 2021, **13**(38), 45670–45678.
4 J. He, L. Cao, J. Cui, G. Fu, R. Jiang, X. Xu, *et al.*, Flexible energy storage devices to power the future, *Adv. Mater.*, 2024, **36**(4), 2306090.
5 S. Hazra, D. Datta, C. Paul, P. K. Roy, S. Sultana, S. Kumar, *et al.*, Electric vehicle integrated tidal-solar-wind-hydrothermal systems for strengthing the microgrid and environment sustainability, *Sci. Rep.*, 2025, **15**(1), 14888.
6 Z. Qin, J. Ma, M. Zhu and T. Khan, Advancements in energy storage technologies: Implications for sustainable energy strategy and electricity supply towards sustainable development goals, *Energy Strategy Rev.*, 2025, **59**, 101710.
7 S. Liu, H. Zhang, X. Peng, J. Chen, L. Kang, X. Yin, *et al.*, Emerging issues and opportunities of 2D layered transition metal dichalcogenide architectures for supercapacitors, *ACS Nano*, 2025, **19**(14), 13591–13636.
8 L. Liu, X. Zhang, Y. Liu and X. Gong, Electrochemical energy storage devices – batteries, supercapacitors, and battery–supercapacitor hybrid devices, *ACS Appl. Electron. Mater.*, 2025, **7**(6), 2233–2270.
9 T. Shaikh, S. Pise, R. Bhosale, M. Vadiyar, K. W. Nam and S. Kolekar, A review and perspective on advancement in metal–organic framework-based composites for supercapacitors: from dimensionalities to functionalities, *Energy Fuels*, 2025, **39**(5), 2396–2421.
10 P. Siddu, K. A. Sree Raj, S. Radhakrishnan, S. Mun Jeong and C. Sekhar Rout, 3D ternary hybrid of VSe_2/e-MXene/CNT with a promising energy storage performance for high performance asymmetric supercapacitor, *Batteries Supercaps*, 2025, **8**(1), e202400466, DOI: 10.1002/batt.202400466.
11 R. Coneo-Rodríguez, A. Y. Tesio, F. P. Cometto, G. M. Morales, G. Á. Planes and A. Caballero, synergetic combination of carbon xerogels, graphene oxide and nano-ZnO for aqueous and organic supercapacitors, *Batteries Supercaps*, 2025, **8**(3), e202400502, DOI: 10.1002/batt.202400502.
12 C. Jiang, H. Liu, J. Ye, N. Wang, Y. Tang, C. He, *et al.*, Recent advances in salt-template assisted synthesis of 3D porous carbon materials for electrochemical energy storage, *Batteries Supercaps*, 2025, **8**(4), e202400563, DOI: 10.1002/batt.202400563.
13 M. A. Puniyanikkottil and S. S. Mal, Polyoxometalate integrated with conducting polymer nanocomposites for supercapacitor and biological sensor applications, *Inorg. Chem.*, 2025, **64**(16), 8222–8237.
14 Y. Zhang, Y. Tan and F. Tuo, In Situ synthesis of vanadium nitride/carbon composites via ice crystal template method-protonated chitosan synergistic strategy for supercapacitors, *ACS Appl. Energy Mater.*, 2025, **8**(18), 13328–13335.
15 S. Ramar, P. Sathish Kumar, M. Govindaraj, M. K. Muthukumaran and B. K. Raja, Morphological tailoring of transition metal tungstate nanoreinforced

composite: A key to unlock high-performance supercapacitors, *Energy Fuels*, 2025, **39**(21), 10070–10082.

16 Z. Fan, T. Xue, Y. Mu, L. Yang, C. Yang, L. Zang, *et al.*, Synergistic enhancement of zinc-ion hybrid capacitors via redox-active doping and sulfonated MXene-modified polypyrrole cathodes, *Adv. Funct. Mater.*, 2025, e10767, DOI: 10.1002/adfm.202510767.

17 R. Zhou and K. Lam, Development of supercapacitors with 3D porous structures, *ChemElectroChem*, 2024, **11**(9), e202300618, DOI: 10.1002/celc.202300618.

18 S. Kaladi Chondath, L. Bansal, B. Sahu and R. Kumar, Dopant-induced defect engineering in transition metal oxide/chalcogenide-based electrodes for high-performance supercapacitors: A Critical Review, *ACS Appl. Energy Mater.*, 2025, 8680–8709.

19 S. Yan, R. Huang, H. Liu and S. Luo, Remarkable conductivity design of $FeCo_2S_4$/MXene 2D membrane electrodes for advanced pseudocapacitance characteristic behavior, *ACS Appl. Energy Mater.*, 2024, **7**(15), 6827–6838.

20 H. Zhong and N. Zhang, A Minireview of multimetallic iron-based oxides for supercapacitive negative electrode materials, *Eur. J. Inorg. Chem.*, 2024, **27**(34), e202400357, DOI: 10.1002/ejic.202400357.

21 M. Saadati pour, M. Delyanee and M. Z. Pedram, Innovative synthesis and advancement strategies for GCN as supercapacitor electrodes: A comprehensive review revealing new insights, *ACS Appl. Energy Mater.*, 2025, **8**(7), 3997–4031.

22 T. Arun, K. Aravinth, P. Balaji Bhargav and M. Govindasamy, Surface sulfurization and self-reconstruction strategy for decorating carbon nanofibers to fabricate sheet-like $NiCo_2S_4$ grown on Ni_3S_2 electrode for high-energy density asymmetric aupercapacitor, *Batteries Supercaps*, 2025, e202400739, DOI: 10.1002/batt.202400739.

23 Z. Molaei, A. A. Asgharinezhad, A. Larimi, C. Ghotbi and F. Khorasheh, Incorporation of CeO_2 nanosheets into $MnCoS_x$ hollow nanorods for next generation supercapacitors, *Energy Fuels*, 2025, **39**(8), 4047–4058.

24 S. Subramani, A. Tamilselvan, G. Rajamanickam and A. Karuppannan, Enhanced electrochemical proficiency of $NiCo_2S_4$/MoS_2/MWCNT hybrid electrodes for superior energy storage applications, *Langmuir*, 2025, **41**(29), 19550–19561.

25 Y. Yue and S. Bian, Nickel cobalt sulfide nanosheets on cotton fabric-derived carbon substrates as self-standing binder-free electrodes for asymmetric all-solid-state supercapacitors, *Battery Energy*, 2025, e70019, DOI: 10.1002/bte2.20240124.

26 A. Narwal, S. K. Mittal, K. Kukreti, A. Khokhar and K. L. Yadav, Engineering $FeCo_2S_4$/MWCNT nanocomposites: a synergistic approach to achieve high energy density in supercapacitors, *J. Energy Storage*, 2025, **124**, 116865.

27 X. Zheng, J. Jiang, T. Bi, F. Jin and M. Li, $FeCo_2S_4$@ Ni@ graphene nanocomposites with rich defects induced by heterointerface engineering for high-performance supercapacitors, *ACS Appl. Energy Mater.*, 2021, **4**(4), 3288–3296.

28 A. Das, A. Mondal and B. B. Khatua, Tuning the electrochemical performance of Cu_2S/Co_3S_4 via optimized CNT incorporation for high energy and high power supercapacitor application, *ACS Appl. Energy Mater.*, 2025, **8**(6), 3812–3825.

29 Y. Liang, J. Gao, Q. Wang, N. Lu, Y. Zhang and X. Zhu, Self-healing micro-supercapacitor based on robust liquid metal-CNT-PEDOT: PSS film for wireless powering of integrated strain sensor, *Small Methods*, 2025, **9**(4), 2401581.

30 S. Fatima, H. Raza, A. Shakoor, F. Saeed, M. Luqman, M. S. Akhtar, *et al.*, Microstructural tailoring for enhanced response of carbon nanotube-filled $BiMnO_3$ electrodes, *Mater. Chem. Phys.*, 2025, **345**, 131198.

31 A. Hussain, A. Tufail, A. Shakoor, M. Mehak, M. S. Akhtar, S. M. Ramay, *et al.*, Synergistically tailored ionic conduction and transport in ZnO/CNTs based electrodes with enhanced electrochemical efficiency in supercapacitors, *Electrochim. Acta*, 2025, **536**, 146736.

32 M. A. M. Elsaid, A. A. Hassan, S. G. Mohamed, A. Z. Sayed, A. M. Ashmawy and A. F. Waheed, Synthesis and electrochemical performance of porous $FeCo_2S_4$ nanorods as an electrode material for supercapacitor, *J. Energy Storage*, 2021, **44**, 103330.

33 A. A. Alamin, M. A. M. Elsaid, A. A. Mansour and W. R. Anis, $FeCo_2S_4$/RGO/Ag diamond-like nanostructured electrode material for highly efficient symmetric supercapacitor, *J. Energy Storage*, 2024, **89**, 111621.

34 A. Shakoor, M. Adnan, M. Luqman, M. A. Khan, S. M. Ramay, F. Ahmad, *et al.*, Synergistic Improvements in Ionic Conductivity, Diffusion Dynamics, and Transference Numbers for $LaNiO_3$/MXene Supercapacitor Electrodes, *Batteries Supercaps*, 2025, **9**(8), e202500014, DOI: 10.1002/batt.202500014.

35 A. Shahzad, M. Saleem, A. Shakoor, M. Z. Manzoor, M. Irfan, S. Atiq, *et al.*, Synergistic electrochemical enhancement of GO-modified MoS_2/ZnO composites for supercapacitor energy storage, *Diamond Relat. Mater.*, 2025, 112908.

36 A. Shahzad, M. Saleem, A. Shakoor, F. Ahmad, S. Atiq, O. Munir, *et al.*, Investigating electrochemical properties in CNT-modified MoS_2/Se composites for supercapacitor electrodes, *J. Power Sources*, 2025, **656**, 238067.

37 M. S. Nadeem, B. Miao, A. Naz, M. Salman, J. Bai, M. A. Al-Tahan, *et al.*, Investigation of synergistically developed p-Co_3O_4/n-ZnHoCuO based junction for enhanced photocatalytic, electrocatalytic, and energy storage applications, *J. Colloid Interface Sci.*, 2025, **699**, 138045.

38 A. Iqbal, R. Nadeem, A. Shakoor, M. Luqman, M. Mehak, M. U. Salman, *et al.*, Enhanced ionic conductivity in synergistically developed $NiMnO_3$/CNTs nanocomposite electrode material in hybrid capacitors, *J. Energy Storage*, 2025, **134**, 118207.

39 A. Shakoor, W. Abbas, M. Hashim, M. Bilal, M. E. Mazhar, S. Atiq, *et al.*, Hierarchical ZnS/MXene Microspheres as Efficient Electrodes for Energy Storage Devices, *Mater. Chem. Phys.*, 2026, 132108.